Large Scale Multi-Period Optimal Power Flow With Energy Storage Systems Using Differential Dynamic Programming

Aayushya Agarwal and Larry Pileggi, *Fellow, IEEE*

Abstract—With the increased penetration of renewable sources, power grids are becoming stressed due to fluctuating generation. To alleviate stress from inconsistent sources, utilities employ energy storage systems alongside renewable sources and rely on dispatching synchronous generators. However, optimal dispatch of such devices is limited by traditional AC optimal power flow methods that do not account for time-dependent constraints, such as the state of charge of energy storage systems and generator ramping constraints. Multi-period optimal power flow is proposed as a large non-convex non-linear problem to optimally dispatch and control generators and energy storage elements across multiple time periods. In this paper, we introduce a scalable, robust framework to solve multi-period optimal power flow using a differential dynamic programming scheme that makes it capable of scaling to large systems containing energy storage devices. We demonstrate the efficacy of this solution by optimizing the SyntheticUSA testcase over a set of time periods. A robust homotopy method is applied to achieve fast simulation times that can be parallelized for further improvements.

Index Terms—Differential dynamic programming, energy storage, multi-period optimal power flow, optimization, steady-state analysis.

NOMENCLATURE

B	Energy storage system state of charge [base = 100 MVA]
$\bar{B}$	Upper bound ESS state of charge [base = 100 MVA]
$\underline{B}$	Lower bound ESS state of charge [base = 100 MVA]
C_d	Discharging cost for ESS [\$/MW]
C_c	Charging cost for ESS [\$/MW]
C_g	Cost for synchronous generation active power production
I_f	Feasibility current source
P_g	Active power of synchronous generator
$\bar{P}_g$	Upper bound of active power of synchronous generator
$\underline{P}_g$	Lower bound of active power of synchronous generator
$\overline{P_{ramp}}$	Upper bound active power ramping constraint
$\underline{P_{ramp}}$	Lower bound active power ramping constraint
$\overline{P_c}$	Active power charging of energy storage system
P_d	Active power discharging of energy storage system
$\overline{P_c}$	Upper Active power charging limit for ESS [base = 100 MW]
$\underline{P_c}$	Lower Active power charging limit for ESS [base = 100 MW]
$\overline{P_d}$	Upper Active power discharging limit for ESS [base = 100 MW]
$\underline{P_d}$	Lower Active power discharging limit for ESS [base = 100 W]
Q_g	Reactive power of synchronous generator
$\overline{Q_G}$	Upper bound of reactive power of synchronous generator
$\underline{Q_G}$	Lower bound of reactive power of synchronous generator
$\mathcal{M}^t$	Network at time, t
V_r	Real component of the bus voltage in pu
V_I	Imaginary component of the bus voltage in pu
X	State vector of optimization including bus real and imaginary voltages, P_G
$\mathcal{L}_{\text{ACOPF}}$	Lagrange function for ACOPF
$\mathcal{L}_{\text{MPOPF}}$	Lagrange function for Multi-Period OPF
η_d	Discharging efficiency for ESS [%]
η_c	Charging efficiency for ESS [%]
γ_{PQ}	SUGAR homotopy factor for loads and generators
$\overline{\mu_{ramp}}$	Slack variable for upper active power ramping constraint of synchronous generators
$\underline{\mu_{ramp}}$	Slack variable for lower active power ramping constraint of synchronous generators

I. INTRODUCTION

THE future of power grid operation is in a state of flux with increasing pressure of implementing renewable sources and decommissioning older polluting generators [1]–[2]. Renewables pose a serious operational challenge due to inconsistent and fluctuating generation that enacts frequency responses by synchronous generators. To subdue these fluctuations, utilities pair renewable sources with energy storage systems (ESS) to better manage renewable power injection into the grid. Future

grid operation relies on optimal management and control of energy storage systems, as well as commissioned synchronous generators, to maintain stability.

Today, operation and planning rely on optimal power flow (OPF) to dispatch the most economic set of generators to meet network demands within device limits. AC-OPF applies AC network constraints to the optimal power flow problem and is heavily researched to achieve robustness and scale to large industry-scale cases. One example software tool is SUGAR (Simulation of Unified Grid Analysis with Renewables), which achieves robustness and scalability using a circuit-theoretic framework and heuristics [20].

While SUGAR is able to solve for the steady-state dispatch given AC network constraints, it only considers a single time period. To account for realistic operation of energy storage systems and generator ramping, it is vital to consider the dispatch across multiple time periods as the charge of energy storage elements and generator ramp limits affect dispatches at all time points. Multi-period optimal power flow (MP-OPF) is an extension of AC-OPF to consider the time-variant properties by optimizing dispatches over multiple time periods. The complexity of multi-period OPF is magnified by the intercoupling of subsequent time periods.

Previous works have identified the challenges in solving multi-period optimal power flow including energy storage devices and modeling the state-of-charge time dependency [3]–[6]. To make the solution process tractable, authors have relaxed the non-linearities with a second order conic relaxations and approximations to the non-linearities [9]–[19]. Many approaches rely on relaxing the non-linearities by assuming DC network constraints or linearized AC constraints [15], [16]. To address the large dimensionality with simulating testcases over multiple periods, other authors have applied Benders' decomposition [7] and differential dynamic approaches [17]. While the previous works have made significant contribution, it remains a challenge to scale MP-OPF solvers to solve large systems, such as the SyntheticUSA testcase [28]. In addition, multi-period optimal power flow is a basis for challenging unit commitment problems that add mixed-integer variables. Authors have attempted to solve a multi-period unit commitment using relaxations to the integer variables [18]–[19], however, dimensionality of multi-period optimal power flow often creates difficulties when trying to scale to large systems. Similarly, an extension to multi-period power flow considers stochastic loads and generation while solving for a dispatch capable of satisfying the network constraints at all time-periods [16]. Previous works have used a multi-stage approach to solve the multi-period OPF in one stage while addressing the stochastic network conditions in another [17]. Overall, a robust multi-period optimal power flow methodology that scales to solve larger systems is imperative to confidently solve more complicated problems such as realistic N-1 multi-period OPF and stochastic multi-period OPF.

We introduce a scalable framework to solve multi-period optimal power flow using differential dynamic programming, which has been shown to aid in multi-period optimizations [22]. Our work builds on the single time period ACOPF engine, SUGAR, and introduces a convergent methodology of differential dynamic programming to solve the multi-period problem. The novelty in adopting a differential dynamic programming approach to solve the grid dispatch for multiple periods achieves a level of scalability capable of solving large systems such as SyntheticUSA testcase. Due to the nature of differential dynamic programming, the framework is able to exploit parallelization for further improvements in simulation to efficiently optimize multiple periods of a large-scale system (approximately 70,000 buses) within an operational simulation time. We devise a new powerful homotopy method to efficiently solve each time period. Compared to existing methodologies [6], [11], we demonstrate the efficiency improvement using a small testcase; however, unlike those methods, our approach is capable of scaling to large systems while considering strict AC network and device constraints.

Section II describes the SUGAR framework that the multi-period optimal power flow is based on and introduces the models for energy storage systems. Section III presents the multi-period optimal power flow formulation and describes the differential dynamic programming approach, along with a parallelization algorithm to achieve faster speedup. The efficacy of the framework is demonstrated in Section IV on large-scale testcases.

II. Optimization Formulation

To construct our multi-period optimization framework, we extend SUGAR AC-OPF, which optimizes operation for a single time period, to incorporate generator ramping limits and models for energy storage systems.

A. Sugar AC-OPF

SUGAR [20] solves AC optimal power flow using circuit-inspired heuristics to robustly find local minima for large systems. Optimizing a single time-period AC-OPF is represented by a Lagrange function with dual and slack variables to represent network equality constraints and device limits respectively, shown in (1).

$$\mathcal{L}_{ACOPF} = \left\| C_g^T P_{g2}^2 \right\| + w_f \left\| I_f \right\|_2^2 + \lambda^T$$
$$(g(X) + I_f) + \mu^T h(X) \tag{1}$$

$g(X)$ is a vector of non-linear equality constraints representing AC current-injection network equations of the grid and λ is a vector of dual variables associated with each equality constraint defined in [20]. Similarly, $h(X)$, explicitly defined in [20], is a vector of inequality constraints representing generator active and reactive power limits, bus voltage bounds and line loading constraints with a vector of corresponding slack variables, μ. Each generator, $i \in G$, produces a certain active power, P_G with an associated quadratic cost C_G. To ensure there is a feasible solution, SUGAR introduces a feasibility current at each node, I_f that is minimized according to a large weight w_f [21]. A feasible optimal dispatch solution will result in all feasible current sources to equal 0 (or within a pre-defined tolerance).

To minimize the cost of generation while meeting network constraints, SUGAR defines a set of the modified Karush-Kuhn-Tucker (KKT) conditions of $\mathcal{L}^{ACOPF}$ (2)-(8), representing the first order optimality conditions to ensure a local minimum is reached. We solve the set of non-linear KKT equations using Newton-Raphson, which provides quadratic convergence properties. During each iteration, Newton-Raphson constructs a Hessian of the $\mathcal{L}^{ACOPF}$.

$$\mathcal{L}_{\text{ACOPF}} = \left\| C_g^T P \right\|_{g_2}^2 + w_f \left\| I_f \right\|_2^2 + \lambda^T \left(g\left(X\right) + \mathrm{I}_f \right) + \mu^T X \tag{2}$$

$$\nabla_\lambda \mathcal{L} = g\left(X\right) + \mathrm{I}_f = 0 \tag{3}$$

$$\nabla_X \mathcal{L} = \nabla_X^T g\left(X\right)\lambda = 0 \tag{4}$$

$$\bar{\mu} \odot \left(X - \bar{X}\right) + \in = 0 \tag{5}$$

$$-\underline{\mu} \odot \left(X - \underline{X}\right) + \in = 0 \tag{6}$$

$$\mu > 0 \tag{7}$$

$$\underline{X} < X < \bar{X} \tag{8}$$

SUGAR applies the following circuit-based limiting heuristics and homotopy methods that can guide the optimization through large-scale solution spaces.

1) Inequality Constraints via Diode Limiting: Inequality constraints are solved using an interior point method that gradually constrains the function shown (9), where the variable x has an upper bound $\bar{x}$ and accompanied with a slack variable μ and constant, $\in$. The interior point method is able to constrain the bounds by gradually decreasing $\in$ (e.g., from 1 to $1e-6$). A lower bound for x is similarly devised.

$$\mu\left(x - \bar{x}\right) + \in = 0 \tag{9}$$

$$\mu > 0 \tag{10}$$

$$x - \bar{x} < 0 \tag{11}$$

Each iteration of the interior point method requires robust limiting to ensure variables do not exceed their operating limits. We employ diode limiting methods that are borrowed from circuit simulation [23] to ensure each primal variable and associated slack variable is individually limited with a factor τ_X and τ_u, respectively (12)–(13) [21].

$$\mu^{k+1} = \mu^k + \tau_u \Delta\mu \tag{12}$$

$$x^{k+1} = x^k + \tau_X \Delta x \tag{13}$$

At the next iteration, the primal and slack variable (x^{k+1}, μ^{k+1}) are damped by τ_X and τ_u (less than or equal to 1) to ensure the variables do not exceed their operating limit during any point (14)–(15). We also include damping constants γ_X and γ_μ of 0.95 to ensure primal and slack variables do not oscillate around their respective limits.

$$\tau_u = \min\left(1, -\gamma_\mu \frac{\mu^k}{\Delta\mu}\right) \tag{14}$$

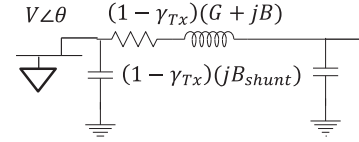$$\tau_X = \min\left(1, \bar{x} - \gamma_X \frac{x^k}{\Delta x}\right) \tag{15}$$

Fig. 1.   Embedding homotopy factor, λ, into linear transmission line elements for Tx-stepping [20].

2) Homotopy Methods: Optimizing future grid operations is challenging in part because of poor initial conditions used for optimization. SUGAR accommodates arbitrary initial conditions by employing a homotopy method that relaxes the non-linear constraints to a trivial problem, $\mathcal{G}(x)$, and then sequentially solves a series of sub-problems to the original problem, $\mathcal{F}(x)$. A scalar homotopy factor, $\gamma \in [0, 1]$, is embedded into the non-linear ACOPF formulation and is iteratively decreased from 1 to 0 to trace a path in the solution space. The resulting homotopy problem is defined by $\mathcal{H}(x, \gamma)$ (16).

$$\mathcal{H}\left(x, \gamma\right) = \left(1 - \gamma\right) \mathcal{F}\left(x\right) + \gamma \mathcal{G}\left(x\right) \\ where \; \gamma \in [0, 1] \tag{16}$$

Specifically, SUGAR embeds the homotopy factor, γ_{Tx}, into linear transmission elements, known as Tx-stepping [20], to virtually short the network as illustrated by Fig. 1. Evidently, at a homotopy factor of 1, the transmission line conductance and susceptance values are 0, thereby shorting the entire system. As the homotopy factor decreases, the system reaches its original configuration.

To relax the inequality constraints, SUGAR also embeds the homotopy factor, γ_{PQ}, into the active (17) and reactive power limits (18) and load values shown in (19)-(20).

$$\left(1 - \gamma_{PQ}\right) \underline{P_G} - \gamma_{PQ} \leq P_G \leq \left(1 - \gamma_{PQ}\right) \overline{P_G} + \gamma_{PQ} \tag{17}$$

$$\left(1 - \gamma_{PQ}\right) \underline{Q_G} - \gamma_{PQ} \leq Q_G \leq \left(1 - \gamma_{PQ}\right) \overline{Q_G} + \gamma_{PQ} \tag{18}$$

$$P_L = P_L \left(1 - \gamma_{PQ}\right) \tag{19}$$

$$Q_L = Q_L \left(1 - \gamma_{PQ}\right) \tag{20}$$

The method above mimics a system with generators and loads ramping up, and has been demonstrated to robustly solve large-scale systems starting from arbitrary initial conditions. The initial trivial problem, denoted by $\gamma_{Tx} = 1$ and $\gamma_{PQ} = 1$, represents a virtually shorted network with no loads.

Each homotopy step uses the solution of the previous step as an initial condition, while a Newton-Raphson solver ensures fast convergence given a small change in the network. This generator stepping, together with Tx-stepping, enables robust convergence of SUGAR formulations for large scale AC-OPF. The overall method to solve a single time-period of AC-OPF with homotopy and diode-limiting is illustrated by the algorithm shown in Fig. 2.

B. Generator Ramping Limits

To facilitate realistic modeling of synchronous generators, we extend SUGAR ACOPF framework to model generator ramping constraints to ensure dispatches are feasible [6]. Given the previous active power set-point of a generator, $P_G^{t-\Delta t}$, the
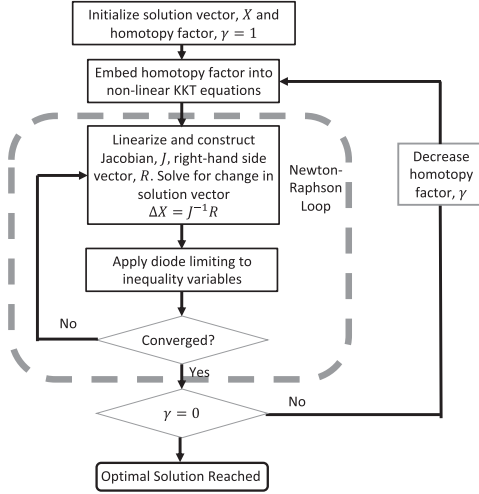
Fig. 2. SUGAR methodology for solving single-time period AC-OPF using homotopy and diode-limiting.

optimal dispatch must ensure that the active power set point meets the lower and upper ramping limits, $\underline{P_{ramp}}$ and $\overline{P_{ramp}}$ as shown in (21). The inequality constraint is integrated into the framework via the interior-point method with corresponding complementary slack variables, $\underline{\mu_{P_{ramp}}}$ and $\overline{\mu_{P_{ramp}}}$ (22)-(24).

$$\underline{P_{ramp}} \leq P_G - P_G^{t-\Delta t} \leq \overline{P_{ramp}} \tag{21}$$

$$\overline{\mu_{P_{ramp}}} \cdot \left(P_G - P_G^{t-\Delta t} - \overline{P_{ramp}}\right) + \epsilon = 0 \tag{22}$$

$$-\underline{\mu_{P_{ramp}}} \cdot \left(P_G - P_G^{t-\Delta t} - \underline{P_{ramp}}\right) + \epsilon = 0 \tag{23}$$

$$\overline{\mu_{P_{ramp}}}, \underline{\mu_{P_{ramp}}} > 0 \tag{24}$$

C. Energy Storage System Model

We further introduce time-variant energy storage system (ESS) models into the SUGAR framework with accompanying constraints on the state of charge. An ESS is constantly charging and discharging power into the grid. During any time period, Δt, the average active and reactive power discharged from an ESS is denoted by P_d and Q_d, whereas the ESS charges an average power of P_c and Q_c.

We extend SUGAR to include real and imaginary ESS current injection, $I_{r,ESS}$ and $I_{i,ESS}$ (25)-(26), where $V_{r,ESS}$ and $V_{i,ESS}$ are the real and imaginary voltages of the ESS bus.

In addition, the state of charge of the ESS, B, is modeled to appropriately consider maximum and minimum charge limits, $\bar{B}$ and $\underline{B}$. The state of charge can be determined by the charge and discharge active power, as well as the state of charge in the previous time step, $B^{t-\Delta t}$, shown in (27) [6]. η_c and η_d are the charging and discharging efficiency of the energy storage device. In addition, (28)-(30) are the interior-point equations modeling the maximum and minimum limits of the ESS charge with corresponding slack variables, $\overline{\mu_{B,ESS}}$ and $\mu_{B,ESS}$, respectively.

As energy storage devices are preferred for this low cost, we amend the Lagrange function to include a linear cost of charging

and discharging, C_c and C_d [6].

$$I_{r,ESS} = \frac{(P_d - P_c)\,V_{r,ESS} - (Q_d - Q_c)\,V_{i,ESS}}{V_{r,ESS}^2 + V_{i,ESS}^2} \tag{25}$$

$$I_{i,ESS} = \frac{(P_d - P_c)\,V_{i,ESS} + (Q_d - Q_c)\,V_{r,ESS}}{V_{r,ESS}^2 + V_{i,ESS}^2} \tag{26}$$

$$B = B^{t-\Delta t} + (\eta_c P_c - \eta_d P_d)\,\Delta t \tag{27}$$

$$\overline{\mu_{B,ESS}} \cdot (B - \bar{B}) + \epsilon = 0 \tag{28}$$

$$-\underline{\mu_{B,ESS}} \cdot (B - \underline{B}) + \epsilon = 0 \tag{29}$$

$$\overline{\mu_{B,ESS}}, \underline{\mu_{B,ESS}} > 0 \tag{30}$$

III. MULTI-PERIOD OPTIMIZATION

The models described for energy storage and generator ramping are inherently time-variant, requiring the state at the previous time period. To properly optimize the behavior of energy storage components or systems, it is vital to consider multiple time periods to ensure the state of charge at all time points are within limits, and generators are ramping within limits. A multi-period optimal power flow solves for the dispatch at each time period while respecting time-varying restrictions (31). Here we consider a time point, t, ranging from 1 to a final period, t_n. A user-defined time step, Δt, discretizes the time scale from 1 to t_n into these integer values denoted by t.

$$\min \sum_{t=1}^{t_n} \left\| P_g^t \right\|_2^2 + \left(C_d P_d^t - C_c P_c^t\right) + I_f^t 2$$

$$s.t\ g^1\left(X^1\right) = 0$$

$$h^1\left(X^1\right) \leq 0$$

$$\underline{P_G} \leq P_G^1 \leq \overline{P_G}$$

$$\underline{B} \leq B^1 \leq \bar{B}$$

$$g^{t_n}\left(X^{t_n}\right) = 0$$

$$h^{t_n}\left(X^{t_n}\right) \leq 0$$

$$P_{min} \leq P_G^{t_n} \leq P_{max}$$

$$\underline{B} \leq B^{t_n} \leq \bar{B}$$

$$B^t = B^{t-\Delta t} + \left(\eta_c P_c^t - \eta_d P_d^t\right)\Delta t$$

$$P_C^t \leq \overline{P_c}$$

$$P_d^t \leq \overline{P_d}$$

$$\underline{P_{ramp}} \leq P_G^t - P_G^{t-\Delta t} \leq \overline{P_{ramp}} \tag{31}$$

The multi-period optimization problem above minimizes the cost of generation for all time periods while ensuring the network is feasible. The Lagrange function, $\mathcal{L}_{MPOPF}$, associated with this constrained optimization, along with the first-order optimality conditions are given below.

$$\mathcal{L}_{\text{MPOPF}} = \sum_{t=1}^{t_n} \left\| C_g^T P_g \right\|_2^2 + \left(C_d P_d^t - C_c P_c^t\right) + I_f^t 2$$

$$+ \sum_{t=1}^{t_n} \lambda^{t^\mathrm{T}} \left(g^t \left(X^t \right) + \mathrm{I}_\mathrm{f}^t \right) + \mu^{t^T} h^t \left(X^t \right) \quad (32)$$

$$\nabla_{\lambda^t} \mathcal{L}_\mathrm{MPOPF} = g^t \left(X^t \right) + \mathrm{I}_\mathrm{f}^t = 0 \quad (33)$$

$$\nabla_{X^t} \mathcal{L}_\mathrm{MPOPF} = \nabla_{X^t}^T g \left(X^t \right) \lambda^t = 0 \quad (34)$$

$$\nabla_{P_G^t} \mathcal{L}_\mathrm{MPOPF} = 2 C_g P_G^t + \nabla_{P_G^t} g^t \left(X^t \right)$$
$$+ \overline{\mu_{P_{ramp}}^t} - \underline{\mu_{P_{ramp}}^t} - \left(\overline{\mu_{P_{ramp}}^{t+\Delta t}} - \underline{\mu_{P_{ramp}}^{t+\Delta t}} \right) \quad (35)$$

$$\nabla_{B^t} \mathcal{L}_\mathrm{MPOPF} = \nabla_{B^t} g^t \left(X^t \right) + \lambda_B^t - \lambda_B^{t+\Delta t} \quad (36)$$

$$\overline{\mu^t} \odot \left(X^t - \bar{X} \right) + \epsilon = 0 \quad (37)$$

$$- \underline{\mu}^t \odot \left(X^t - X \right) + \epsilon = 0 \quad (38)$$

$$\mu^t > 0 \quad (39)$$

$$X < X^t < \bar{X} \quad (40)$$

Interestingly, the Lagrange function for the multi-period optimal power flow is comparable to the Lagrange function of the AC-OPF of each time period. Without any generator ramping constraints or ESS time-varying constraints in (31), the multi-period Lagrange function is identical to the summation of all the AC-OPF Lagrange functions shown in (41).

$$\mathcal{L}_\mathrm{MPOPF} = \sum_{t=1}^{t_n} \mathcal{L}_{ACOPF}^t + \sum_{t=2}^{t_n} \overline{\mu_{P_{ramp}}^t}.$$
$$\left(P_G^t - P_G^{t-\Delta t} - \overline{P_{ramp}} \right) - \underline{\mu_{P_{ramp}}^t} \cdot \left(P_G^t - P_G^{t-\Delta t} - \underline{P_{ramp}} \right)$$
$$+ \sum_{t=2}^{t_n} \lambda_B^t \left(B^t - \left(B^{t-\Delta t} + \left(\eta_c P_c - \eta_d P_d \right) \Delta \mathrm{t} \right) \right) \quad (41)$$

However, the added generator ramping constraints and ESS state of charge equations couple each subsequent time period together. From the KKT conditions in (42)-(46), the coupling variables between time periods are the active power of generators, the ramp constraint slack variables and ESS state of charge. In those equations, the red variables denote variables from the preceding time period and the blue variables indicate contributions from the following time period. Importantly, the KKT conditions couple the active power with the preceding (43)-(44) time steps. Similarly, the ESS equations are coupled with the previous state of charge, $B^{t-\Delta t}$ (45), and future dual variables, $\lambda_B^{t+\Delta t}$ (46).

$$\nabla_{P_G^t} \mathcal{L}_{MPOPF} = \nabla_{P_G^t} \mathcal{L}_{ACOPF} + \left(\overline{\mu_{P_{ramp}}^t} - \underline{\mu_{P_{ramp}}^t} \right)$$
$$- \left(\overline{\mu_{P_{ramp}}^{t+\Delta t}} - \underline{\mu_{P_{ramp}}^{t+\Delta t}} \right) \quad (42)$$

$$\overline{\mu_{P_{ramp}}^t} \cdot \left(P_G^t - P_G^{t-\Delta t} - \overline{P_{ramp}} \right) + \epsilon = 0 \quad (43)$$

$$- \underline{\mu_{P_{ramp}}^t} \cdot \left(P_G^t - P_G^{t-\Delta t} - \underline{P_{ramp}} \right) + \epsilon = 0 \quad (44)$$

$$\nabla_{\lambda_B^t} \mathcal{L}_{MPOPF} = B^t - \left(B^{t-\Delta t} + \left(\eta_c P_c - \eta_d P_d \right) \Delta t \right) \quad (45)$$

$$\nabla_{B^t} \mathcal{L}_{MPOPF} = \lambda_B^t - \lambda_B^{t+\Delta t} + \overline{\mu_{B,ESS}^t} - \underline{\mu_{B,ESS}^t} \quad (46)$$

In order to solve for an optimal sequence of control actions representing generator power dispatches during each time period, we employ a differential dynamic programming approach (DDP). DDP generates the cost associated to a feasible control sequence by simulating the grid dynamics during the forward pass, as described by (41). The forward pass optimizes the dispatch of each time period separately using forward substitution for previous time variables and fixed constants for future variables. Once the forward sequence is complete, DDP performs a backward pass to update the sequence based on gradient information from the forward trajectory. The combination of a forward pass and backward pass produces a new sequence of controls [22]. At convergence, the backward pass does not affect the forward trajectory, thereby indicating that the algorithm has reached a minimum.

A. DDP Forward Pass

During the forward pass, the framework optimizes each time period sequentially, and considers the effect of time-varying restraints in the forward time direction. Each time period optimizes the dispatch of generators and ESS while considering the set points and ESS charge at the previous time period as constants using the framework given in Fig. 2. The Lagrange function associated with this optimization at a time, t, denoted $\mathcal{L}_{MPOPF}^t$, is formulated as

$$\mathcal{L}_{MPOPF}^t = \mathcal{L}_{ACOPF}^t + \overline{\mu_{P_{ramp}}^t} \cdot \left(P_G^t - P_G^{t-\Delta t} - \overline{P_{ramp}} \right)$$
$$- \underline{\mu_{P_{ramp}}^t} \cdot \left(P_G^t - P_G^{t-\Delta t} - \underline{P_{ramp}} \right)$$
$$- P_G^t \left(\overline{\mu_{P_{ramp}}^{t+\Delta t}} - \underline{\mu_{P_{ramp}}^{t+\Delta t}} \right)$$
$$+ \lambda_B^t \left(B^t - \left(B^{t-\Delta t} \right. \right.$$
$$\left. \left. + \left(\eta_c P_c - \eta_d P_d \right) \Delta t \right) - \lambda_B^{t+\Delta t} B^t \right) \quad (47)$$

(47) considers the previous active power set point, $P_G^{t-\Delta t}$ and ESS state of charge, $B^{t-\Delta t}$, as constants obtained from the previous time period's optimal dispatch. Variables from subsequent time periods $\left(\overline{\mu_{P_{ramp}}^{t+\Delta t}}, \underline{\mu_{P_{ramp}}^{t+\Delta t}}, \lambda_B^{t+\Delta t} \right)$ are also constant and will be updated from the backward pass as gradient information. The future variables indicate a change in the optimal dispatch based on ramping violations or state of charge violations from future time periods. However, these variables can only be updated once the forward trajectory is complete. The initial forward trajectory will set each of these future variables to be 0, representing no contribution from subsequent time periods. Once the solution is found for time step, t, the active power set points, P_G^t, and ESS state of charge, B^t, are passed to the following time step.

Performing an ACOPF-like optimization (47) during each forward pass using the homotopy method outlined in the previous section using SUGAR can be computationally expensive. To initiate the framework during the first forward pass, the first time period will require a robust ACOPF solver that can accommodate arbitrary initial conditions. A lack of good initial conditions is common for future grid planning where atypical generation portfolios and network configurations produce varying states.
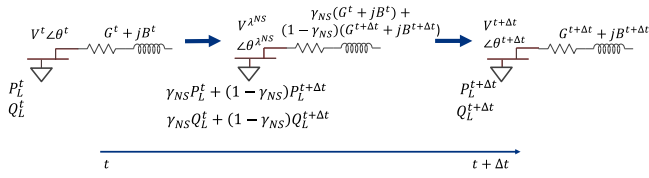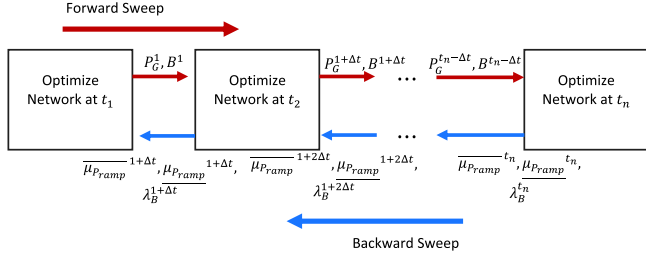
Fig. 3. Network Stepping Method with embedded homotopy factor, γ_{NS}.

Fig. 4. Differential Dynamic Approach for Multi-Period OPF.

However, each subsequent time-period will have similar network conditions with slightly varying load and transmission line switch configurations. To exploit the search space exploration, we use the solution of the previous time step as an initial condition. Generally, the network change between subsequent time periods is gradual enough to exploit Newton-Raphson quadratic convergence characteristics. However, in cases where the Newton-Raphson begins to diverge, we apply a robust homotopy method.

1) Network Stepping: Given a network at time t, $\mathcal{M}^t$ and the corresponding optimal dispatch, X^t, we introduce a homotopy method to determine the state vector at the following time period, $X^{t+\Delta t}$ of the network $\mathcal{M}^{t+\Delta t}$. In general, the network $\mathcal{M}^{t+\Delta t}$ is comprised of loads and linear elements such as transmission lines. Subsequent time periods often see a change in load power values as well as the line impedance switching. Instead of robustly solving for $X^{t+\Delta t}$ using the homotopy methods described in the previous section, we present a network-stepping homotopy method that uses the previous time period's solution as an initial condition and iteratively solves sub-problems leading to the optimal dispatch of $\mathcal{M}^{t+\Delta t}$. Denoting a homotopy factor, γ_{NS} that begins at a value of 1 and iteratively decreases to 0, we characterize the subproblems as:

$$\mathcal{M}^{t+\Delta t}\left(\gamma_{NS}\right) = \gamma_{NS}\,\mathcal{M}^t + (1-\gamma_{NS})\,\mathcal{M}^{t+\Delta t} \qquad (48)$$

Intuitively, loads are gradually changing from their values (P_L, Q_L) at time t and gradually changing to their values at the following time point, $t + \Delta t$. In addition, linear elements that are gradually switching on or off with conductances and susceptances $(G + jB)$ iteratively linearly changing with γ_{NS}, shown in Fig. 3 .

Using the solution from the previous homotopy step, the network change from $\mathcal{M}^t$ to $\mathcal{M}^{t+\Delta t}$ is reduced to a series of sub-problems and is robustly solved with few iterations.
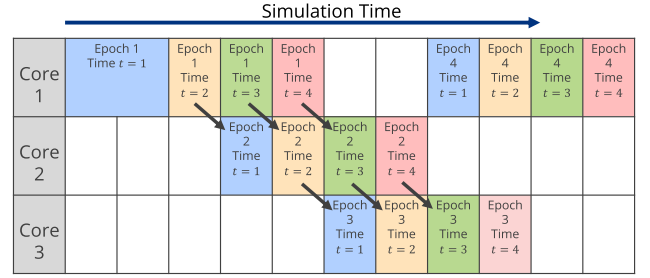
Fig. 5. Scheduling Procedure for parallelizing MP-OPF execution on three cores for four time-periods with a $\Delta t = 1$.

B. DDP Backward Pass

Once the cost of a forward trajectory is constructed, the backward pass is responsible for solving for the gradients that will update the variables for the next forward trajectory. The cost function of the entire trajectory is given by (47). The gradients of the cost function with respect to the coupling variables (P_G^t and B^t) are given below.

$$\nabla_{P_G^t}\,\mathcal{L}_{MPOPF} = \nabla_{P_G^t}\,\mathcal{L}_{APOPF}^t$$
$$- \left(\overline{\mu_{P_{ramp}}}^{t+\Delta t} - \underline{\mu_{P_{ramp}}}^{t+\Delta t}\right) \qquad (49)$$

$$\nabla_{B^t}\,\mathcal{L}_{MPOPF} = \nabla_{B^t}\,\mathcal{L}_{ACOPF}^t - \lambda_B^{t+\Delta t} \qquad (50)$$

The backward pass is responsible for updating the constants $\overline{\mu_{P_{ramp}}}^{t+\Delta t}, \underline{\mu_{P_{ramp}}}^{t+\Delta t}, \lambda_B^{t+\Delta t}$ by passing the values backward in time, shown in the figure below.

C. Parallelizing Epochs

While the forward and backward pass in the present form require few iterations, it is possible to capitalize on parallelism to reduce overall run time. Due to ramping constraints and ESS charge, the differential dynamic approach often requires multiple epochs. An epoch is comprised of a single forward and backward pass. The forward pass of each epoch requires the backward pass of the previous epoch to indicate changes based on the gradient.

The weak coupling between time periods allows for the gradients required for the backward pass at time t to be calculate immediately after the forward pass for time $t + \Delta t$. This allows for the forward trajectory at time t of the following epoch to begin once the current epoch has completed the forward trajectory of time $t + \Delta t$. This paradigm enables the use of parallel processing to run each epoch with minimal information being exchanged. Scheduling the paradigm requires staggering the execution times to wait for the gradient information from the previous epoch. A visual demonstration of the scheduling is shown in Fig. 5.

Fig. 5 demonstrates the parallelization that is possible for optimizing a grid over four time-periods over four epochs on a three-core machine. Each arrow represents passing gradients to the following epoch on a separate machine. Depending on the number of processors available, each core may be required to perform multiple epochs, as shown by Core 1 in Fig. 5.
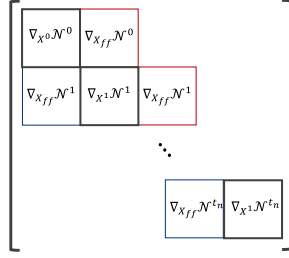
Fig. 6. Coupled block diagonal Hessian with blue blocks representing feedback and red blocks representing feedforward terms.

D. DDP Convergence Analysis

Differential dynamic programming offers a scalable methodology to optimize each time period while respecting temporal dependencies. While proceeding forward through time, DDP optimizes each network relying on past network conditions to ensure a feasible dispatch. During the backward pass, each time period utilizes gradients from future time periods to adjust its own dispatch and optimize the dispatch across all time-coupled time periods.

An analogous methodology is used in timing analysis of MOS circuits [24]–[25] and with decomposition techniques in circuit simulation [26]. Instead of optimizing the network over T time periods, consider T network coupled with each other (not in time but rather in space), each with network configurations, $\mathcal{N}^t$, where $\mathcal{N}^t$ is a network describing the first order optimality conditions of (33)-(40). The network $\mathcal{N}^t$ is a combination of $\mathcal{M}^t$ (the primal network) and its corresponding adjoint, or dual, network (34)-(40).

The coupling between each network, $\mathcal{N}^t$ is represented by the coupling (45), where t now refers to the network rather than time period. In this context, differential dynamic programming decomposes and sequentially optimizes each time-network separately. In the "forward pass", a network, $\mathcal{N}^t$ passes its coupled variables to the following network, $\mathcal{N}^{t+\Delta t}$. In the backward pass, the network $\mathcal{N}^{t+\Delta t}$ then shares its solved variables to the previous network $\mathcal{N}^t$.

The Hessian associated with the entire coupled network can be viewed as a large block diagonal matrix in Fig. 6, with each block representing the first order optimality condition for a single network, $\mathcal{N}^t$. The off-diagonal terms (feedforward coupling $\nabla_{X_{ff}}\mathcal{N}^t$ and feedback coupling $\nabla_{X_{fb}}\mathcal{N}^t$) represent generator ramping constraints and energy storage charges that couple successive networks together. From this perspective, differential dynamic programming is analogous to partitioning networks by tearing the coupling variables present in (45)-(46). After partitioning the network in time, previous methods [24]–[26] use Gauss-Seidel to sequentially solve for each partitioned network using the updated variables from the previous network. During each iteration k in Gauss-Seidel, a network, $\mathcal{N}_k^t$ receives a set of coupling variables, known as feedforward variables, from the previous network at the current iteration, $\mathcal{N}_k^{t-\Delta t}$. In addition, a partitioned network, $\mathcal{N}_k^t$, will consider the coupling from future networks, known as feedback variables, from the

previous Gauss-Seidel iteration, $\mathcal{N}_{k-1}^{t+\Delta t}$. Using relaxation techniques [26], we can denote feedforward variables as X_{ff}^t and feedback variables as X_{fb}^t, which are a subset of the variables of a time-network, X^t. The Gauss-Seidel approach is analogous to differential dynamic programming, with the feedforward and feedback variables defined by:

$$X_{ff}^t = \left\{ P_G^t, \ B^t \right\} \subset X^t \tag{51}$$

$$X_{fb}^t = \left\{ \overline{\mu_{P_{ramp}}}^t, \underline{\mu_{P_{ramp}}}^t, \lambda_B^t \right\} \subset X^t \tag{52}$$

After establishing an equivalent approach between differential dynamic programming and Gauss-Seidel, we can adopt the convergence criteria used for Gauss-Seidel to demonstrate global convergence for DDP. The solution matrix associated to the entire coupled problem is given below

$$\mathcal{H} \begin{bmatrix} X^t \\ X^{t+\Delta t} \\ \vdots \end{bmatrix} = J \equiv \begin{bmatrix} \nabla_\lambda \mathcal{L}^t \\ \nabla_X \mathcal{L}^t \\ \nabla_\lambda \mathcal{L}^{t+\Delta t} \\ \nabla_X \mathcal{L}^{t+\Delta t} \\ \vdots \end{bmatrix} \tag{53}$$

where $\mathcal{H}$ is a coupled block diagonal Hessian shown in Fig. 6. We can further define the Hessian as

$$\mathcal{H} = W - V \tag{54}$$

where W represents the block diagonal elements of the Hessian and V represents the coupling terms. A strict requirement of Gauss-Seidel is the spectral radius of $p(W^{-1}V) < 1$. However, a milder condition is that the Hessian, $\mathcal{H}$ is strictly positive definite. Each block within W represents the linearized form of the network, $\mathcal{N}^t$. The analysis by the authors in [21] and the homotopy methods outlined in previous section conclude that the solution of AC-OPF in each block diagonal within W is positive-definite, as [21] demonstrate guaranteed convergence of the network to a minimum. This property implies that W is positive definite. However, $\mathcal{H}$ relies not only on the block diagonal W, but also on the coupling variables V. Therefore, by demonstrating that the coupling equations V do not affect the positive definiteness of $\mathcal{H}$, then the Gauss-Seidel algorithm is guaranteed to converge.

The equations coupling the block diagonal elements together, (42) and (45), represent generator ramping and ESS state of charge, respectively. To ensure positive definiteness is maintained, we demonstrate that the linearized form of the (42), reproduced below, is diagonally dominant.

$$\nabla_{P_G^t}\mathcal{L} = w * 2C_G^T P_G^t + \lambda^{t^T} \nabla_{P_G^t} g^t \left(X^t \right)$$

$$+ \left(\overline{\mu_{P_{ramp}}}^t - \underline{\mu_{P_{ramp}}}^t \right)$$

$$- \left(\overline{\mu_{P_{ramp}}}^{t+\Delta t} - \underline{\mu_{P_{ramp}}}^{t+\Delta t} \right) \tag{55}$$

To ensure that the cost function in (42) is diagonally dominant, we scale the entire objective by w, as shown in (55). The value of w is chosen such that by adding the additional slack variables associated to the ramping constraint (which have a magnitude
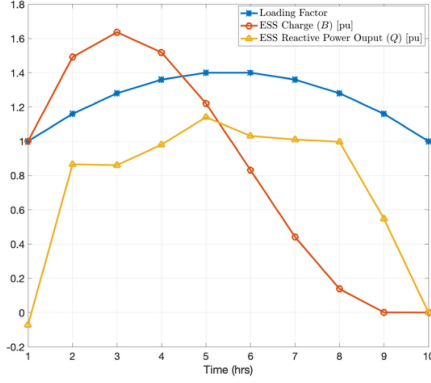
Fig. 7. IEEE-14 Testcase Multi-Period OPF with ESS on Bus 2 with Blue curve describing load factor and orange curve describing ESS state of charge.

of 1 in the Hessian) the value of $w * 2C_G^T \geq \sum_{i \neq j} |a_{ij}|$, where a_{ij} are the terms in the Hessian corresponding to (55). Of course, a large scaling factor, w, may create numerical conditioning issues that could hinder convergence [27].

Now to ensure that (45) is also diagonally dominant, we introduce a new (56) to define the coupling between time periods and substitute the variable, ΔB^t appropriately into (57). By scaling the variable, ΔB^t in (56) by 2, we can ensure (56) is diagonally dominant.

$$2\Delta B^t - \left(B^t - B^{t-\Delta t}\right) = 0 \qquad (56)$$

$$2\Delta B^t - (\eta_c P_c - \eta_d P_d)\Delta t = 0 \qquad (57)$$

For (57) to be diagonally dominant we ensure that $\Delta t \leq 2/(\eta_C + \eta_d)$. Together, by choosing an appropriate cost scaling factor, w and a time period, Δt, we are able to ensure convergence of Gauss-Seidel that partitions the network in time, which we previously have shown to be identical to differential dynamic programming.

IV. RESULTS

The efficiency and validity of the DDP framework is demonstrated by solving a small 14-bus system which is compared against fmincon [29]. To demonstrate the scalability and efficacy of the parallelization framework, we also solve a large SyntheticUSA testcase in operational time.

A. Energy Storage Devices in IEEE-14 Bus Testcase

The IEEE-14 bus testcase is modified to include energy storage devices using our framework. The generator at bus 2 is replaced with an energy storage system with parameters shown in the table below. The base quantities and description for each parameter is described in the Nomenclature section.

The 14-bus system is optimized over 10 hourly time periods with loading factor varying throughout the simulation, as shown by the blue curve in Fig. 7. The loading factor value is multiplied by the active and reactive power injection value of each load in the IEEE 14 bus case at each time. The loading factor following

TABLE I
IEEE-14 BUS ENERGY STORAGE DEVICE PARAMETERS

η_c	η_d	C_c	C_d	$\bar{B}$	$\underline{B}$	$\bar{P_c}$	$\underline{P_c}$	$\bar{P_d}$	$\underline{P_d}$
0.85	0.85	0.01	0.001	5pu	0pu	1pu	0pu	1pu	0pu

TABLE II
ITERATION COUNT FOR MULTI-PERIOD SUGAR AND FMINCON [29] SOLVING MODIFIED IEEE-14 BUS CASE

	Multi-Period SUGAR	fmincon [29]
Iterations	43	367

a simple distribution given by the equation:

$$lf\ (t) = 1 - 0.02 * t * (t - 10) \qquad (58)$$

$where\ t\ =\ \{1, 2, \ldots, 10\}$

Over the course of three epochs, the ESS state of charge changes to find the optimal dispatch of the synchronous generators and energy storage elements represented by the red and orange curve on Fig. 7.

Importantly, we notice that the optimal dispatch of the ESS at bus 2 is to charge the device during the initial time periods with low loading and discharge during the higher loading time periods. Since the cost of discharging of the ESS device is much lower than the cost of power produced by synchronous generators, the ESS can compensate during high loading periods. However, the ESS device does not dissipate its entire charge immediately due to ramping constraints of the other synchronous generators in the network. If the ESS were to discharge rapidly, the synchronous generators would have to ramp down their active power production and subsequently ramp up once the ESS is fully discharged. However, the generator ramping constraints prohibits this rapid ramping behavior.

1) Comparison With Matlab Fmincon [29]: To validate our approach, we compare the modified IEEE-14 bus case with the Matlab optimization tool, fmincon [29]. In the comparison, the entirety of the multi-period optimization problem (31) is solved using fmincon's interior-point method and default parameter values. The results from fmincon match with the results shown in Fig. 6 within a tolerance of a norm square error of $1e - 5$, but there is a stark difference in robustness as evidenced by the iteration count shown in Table II. Both multi-period SUGAR and fmincon were initialized with AC-OPF solutions of the base case and ran on a single core of a Macbook Pro 2.6 GHz Intel Corei7.

The data for the modified IEEE-14 bus testcase is publicly available at [30]. The result validates differential dynamic methodology to solve the multi-period problem.

B. MP-OPF for SyntheticUSA

To demonstrate the scalability of the framework, we optimize the dispatch across multiple time periods of the large, 70 k+ bus SyntheticUSA testcase that represents the behavior of the US grid [28]. Accompanying the testcase, the dataset includes a synthetic hourly load demand for January 6th, 2016. In this experiment, the grid was optimized over 10 time periods (hours) using the load profile from 8 am to 6 pm on January 6, 2016. Each generator was further constrained with ramp rates of 5%
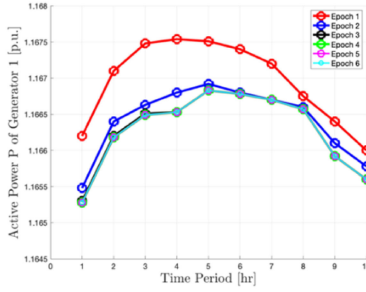
Fig. 8. Active Power Generation for Generator 10001 in SyntheticUSA over multiple epochs and time-periods.
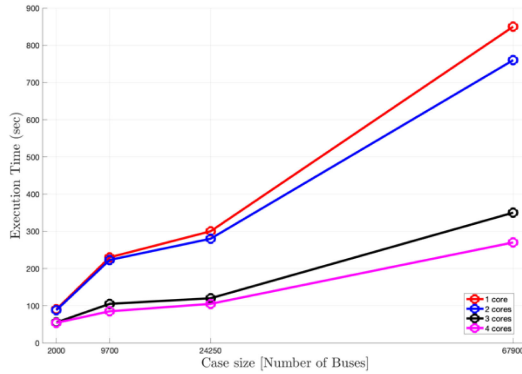

Fig. 9. Execution time of MP-OPF for Synthetic testcases on multiple cores.

and active and reactive power limits defined by the testcase. The system is initialized by flat start (1.0 pu voltage and 0 degrees) to highlight the robustness. Fig. 8 demonstrates the differential dynamic process as generator 10001 is changing its trajectory during each epoch to minimize the total cost of generation while also maintaining ramp rate limits.

The specific generator at bus 10001 is able to converge to the desired solution in three epochs. The framework optimizes the entire dispatch of SyntheticUSA in six epochs from flat start. Using a single core on a Macbook Pro 2.6 GHz Intel Corei7, the entire process took 14 minutes.

C. Scalability Study

The framework is also demonstrated on various synthetic testcases with the range of buses shown in Fig. 9 [28]. The largest testcase is the SyntheticUSA grid with 67900 buses and 8107 time-variant synchronous generators that capable of ramping. Each testcase is optimally dispatched over 10 hours and initialized from a flat start (a bus voltage magnitude of 1.0 pu and angle of 0 pu). The execution time shown in Fig. 9 includes parsing as well as execution for the differential dynamic approach. To further improve simulation times, the framework is parallelized using the scheduling algorithm outlined in Section III. Using a MacbookPro with 2.6 GHz Intel Corei7, the framework was parallelized up to 4 separate cores. A detailed description of the speedup achieved through parallelism for the largest SyntheticUSA testcase is highlighted in Table III. Evidently, parallelism offers a benefit to the speedup using the scheduling algorithm outlined earlier. To solve larger systems of scale comparable

TABLE III
SPEEDUP OF MULTI-PERIOD OPF OF SYNTHETICUSA TESTCASE ACROSS NUMEROUS CORES

Cores	1	2	3	4
Speedup	1.0	1.12	2.52	3.23

to the SyntheticUSA, we would utilize parallelism to achieve a result within a realistic operation window of 5 minutes. The results in Fig. 9 indicate that 4 cores are able to reduce the execution time to less than 5 minutes while considering all strict AC constraints. Additional hardware for greater parallelism would benefit execution time of larger studies.

V. CONCLUSION

Planning for future grid operations will heavily rely on optimal management of energy storage devices and synchronous generators to ensure stability in the midst of emerging renewable sources. A robust and scalable multi-period optimization, as presented in this paper, is required to study dispatches while considering AC network constraints. By using a differential dynamic approach, we present a framework to optimize dispatches of large systems of up to 70k buses across multiple time periods. A parallel scheduling algorithm is also introduced to allow further speedup. The framework offers planning engineers a robust tool to study the optimal management for future generation portfolios. The robust multi-period framework lays a foundation for exploring large-scale optimization studies such as unit commitment that include temporal effects.

REFERENCES

[1] X. Li and S. Wang, "A review on energy management, operation control and application methods for grid battery energy storage systems," *CSEE J. Power Energy Syst.*, 2019.

[2] S. O. Showers and A. K. Raji, "Benefits and challenges of energy storage technologies in high penetration renewable energy power systems," in *Proc. IEEE PES/IAS PowerAfrica*, Abuja, Nigeria, 2019.

[3] N. Savvopoulos, C. Y. Evrenosoglu, A. Marinakis, A. Oudalov, and N. Hatziargyriou, "A long-term reactive power planning framework for transmission grids with high shares of variable renewable generation," in *Proc. IEEE Milan PowerTech*, Milan, Italy, Jun. 2019 pp. 1–6.

[4] J. F. Marley, D. K. Molzahn, and I. A. Hiskens, "Solving multiperiod OPF problems using an AC-QP algorithm initialized with an SOCP relaxation," *IEEE Trans. Power Syst.*, vol. 32, no. 5, pp. 3538–3548, Sep. 2017.

[5] J. Sun, X. Li, and H. Ma, "Study on optimal capacity of multi-type energy storage system for optimized operation of virtual power plants," in *Proc. China Int. Conf. Electricity Distrib.*, Tianjin, Sep. 2018, pp. 2989–2993.

[6] Z. Wang, J. Zhong, D. Chen, Y. Lu, and K. Men, "A multi-period optimal power flow model including battery energy storage," in *Proc. IEEE Power Energy Soc. Gen. Meeting*, Jul. 2013, pp. 1–5.

[7] A. Rabiee and M. Parniani, "Voltage security constrained multi-period optimal reactive power flow using benders and optimality condition decompositions," *IEEE Trans. Power Syst.*, vol. 28, no. 2, pp. 696–708, May 2013.

[8] T.-H. Kim, H.-S. Shin, H.-T. Kim, S.-W. Lee, and W. Kim, "A multi-period optimal power flow algorithm for microgrid in consideration with the state-of-charge of BESS's," in *Proc. IEEE Transp. Electrific. Conf. Expo., Asia-Pacific*, Busan, Jun. 2016, pp. 635–640.

[9] Á. Lorca and X. A. Sun, "The adaptive robust multi-period alternating current optimal power flow problem," *IEEE Trans. Power Syst.*, vol. 33, no. 2, pp. 1993–2003, Mar. 2018.

[10] O. Mégel, J. L. Mathieu, and G. Andersson, "Hybrid stochastic-deterministic multiperiod DC optimal power flow," *IEEE Trans. Power Syst.*, vol. 32, no. 5, pp. 3934–3945, Sep. 2017.

[11] R. A. Jabr, S. Karaki, and J. A. Korbane, "Robust multi-period OPF with storage and renewables," *IEEE Trans. Power Syst.*, vol. 30, no. 5, pp. 2790–2799, Sep. 2015.

[12] I. I. Avramidis, F. Capitanescu, and G. Deconinck, "A tractable approximation approach to deal with the binary nature of shiftable loads in multi-period optimal power flow," in *Proc. IEEE Texas Power Energy Conf.*, College Station, TX, USA, Mar. 2020, pp. 1–6.

[13] W. Bai and K. Y. Lee, "Modified optimal power flow on storage devices and wind power integrated system," in *Proc. IEEE Power Energy Soc. Gen. Meeting*, Boston, MA, USA, Jul. 2016, pp. 1–5.

[14] N. Meyer-Huebner, M. Suriyah, and T. Leibfried, "N-1-secure optimal generator redispatch in hybrid AC-DC grids with energy storage," in *Proc. IEEE PES Innov. Smart Grid Technol. Conf. Europe*, Sarajevo, Oct. 2018, pp. 1–6.

[15] J. Cao, W. Du, and H. F. Wang, "An improved corrective security constrained OPF with distributed energy storage," *IEEE Trans. Power Syst.*, vol. 31, no. 2, pp. 1537–1545, Mar. 2016.

[16] R. A. Jabr, S. Karaki, and J. A. Korbane, "Robust multi-period OPF with storage and renewables," *IEEE Trans. Power Syst.*, vol. 30, no. 5, pp. 2790–2799, Sep. 2015, doi: 10.1109/TPWRS.2014.2365835.

[17] J. C. López, P. P. Vergara, C. Lyra, M. J. Rider, and L. C. P. da Silva, "Optimal operation of radial distribution systems using extended dynamic programming," *IEEE Trans. Power Syst.*, vol. 33, no. 2, pp. 1352–1363, Mar. 2018.

[18] Y. Cho, T. Ishizaki, N. Ramdani, and J. Imura, "Box-based temporal decomposition of multi-period economic dispatch for two-stage robust unit commitment," *IEEE Trans. Power Syst.*, vol. 34, no. 4, pp. 3109–3118, Jul. 2019.

[19] A. İ. Mahmutoğulları, S. Ahmed, Ö. Çavuş, and M. S. Aktürk, "The value of multi-stage stochastic programming in risk-averse unit commitment under uncertainty," *IEEE Trans. Power Syst.*, vol. 34, no. 5, pp. 3667–3676, Sep. 2019.

[20] A. Pandey, A. Agarwal, and L. Pileggi, "Incremental model building approach for solving exact AC-constrained optimal power flow," in *Proc. Hawaii Int. Conf. System Sci. (Submitted)*, 2021. [Online]. Avilable: https://doi.org/10.24251/HICSS.2021.398

[21] M. Jereminov, D. M. Bromberg, A. Pandey, M. R. Wagner, and L. Pileggi, "Evaluating feasibility within optimal power flow," *IEEE Trans. Smart Grid*, vol. 11, no. 4, pp. 3522–3534, Jul. 2020.

[22] X. Qian and Y. Zhu, "Differential dynamic programming for multistage uncertain optimal control," in *Proc. 7th Int. Joint Conf. Comput. Sci. Optim.*, Beijing, 2014, pp. 88–92.

[23] L. Pillage(Pileggi), R. Rohrer, and C. Visweswariah, *Electronic Circuit & System Simulation Methods*. New York, NY, USA: McGraw-Hill, 1995.

[24] G. De Micheli and A. Sangiovanni-Vincentelli, *Numerical Properties of Algorithms for the Timing Analysis of MOS VLSI Circuits*. Univ. of California Berkeley ERL Memo, May 1981.

[25] N. Rabbat, A. Sangiovanni-Vincentelli, and H. Hsieh, "A multilevel Newton algorithm with macromodeling and latency for the analysis of large-scale nonlinear circuits in the time domain," *IEEE Trans. Circuits Syst.*, vol. 26, no. 9, 1979.

[26] M. P. Desai and I. N. Hajj, "On the convergence of block time-point relaxation methods for circuit simulation," Coordinated Sci. Lab. Rep. No. UILU-ENG-88-2209, DAC-11, 1988.

[27] W. Andreas and B. Lorenz, "On the implementation of an interior-point filter line-search algorithm for large-scale nonlinear programming.," *Math. Program.*, vol. 106, no. 1, pp. 25–57, 2006.

[28] A. B. Birchfield, T. Xu, K. M. Gegner, K. S. Shetye, and T. J. Overbye, "Grid structural characteristics as validation criteria for synthetic networks," *IEEE Trans. Power Syst.*, vol. 32, no. 4, pp. 3258–3265, Jul. 2017.

[29] C. Josz, S. Fliscounakis, J. Maeght, and P. Panciatici, AC Power Flow Data in MATPOWER and QCQP Format: iTesla, RTE Snapshots, and PEGASE, 2016. [Online]. Avilable: http://arxiv.org/abs/1603.01533

[30] A. Agarwal, "Multi-Period OPF Cases," 2020. [Online]. Available: https://github.com/Aayushya-Agarwal/Multi-Period-OPF-cases

Aayushya Agarwal was born in Sirsa, India. He received the B.Sc. degree in electrical engineering with a computer engineering minor from the University of Waterloo, Canada, in 2017 and is currently working toward the Ph.D. degree in electrical and computer engineering with Carnegie Mellon University, Pittsburgh, USA. His research interests include optimization, simulation, and modeling of electrical power systems.

LarryPileggi (Fellow, IEEE) received the Ph.D. degree in electrical and computer engineering from Carnegie Mellon University, Pittsburgh, USA, in 1989. He is the Tanoto Professor and Head of electrical and computer engineering with Carnegie Mellon University, and has previously held positions with Westinghouse Research and Development and the University of Texas at Austin. He has coauthored "Electronic Circuit and System Simulation Methods," McGraw-Hill, 1995 and "IC Interconnect Analysis," Kluwer, 2002. He has authored or coauthored more than 400 conference and journal papers and holds 40 U.S. patents. His research interests include various aspects of digital and analog integrated circuit design, and simulation, optimization and modeling of electric power systems. He was the Co-Founder of Fabbrix Inc., Extreme DA, and Pearl Street Technologies. He was the recipient of the various Awards, including Westinghouse Corporation's highest engineering achievement Award, the Semiconductor Research Corporation (SRC) Technical Excellence Awards in 1991 and 1999, the FCRP inaugural Richard A. Newton GSRC Industrial Impact Award, the SRC Aristotle award in 2008, the 2010 IEEE Circuits and Systems Society Mac Van Valkenburg Award, the ACM/IEEE A. Richard Newton Technical Impact Award in Electronic Design Automation in 2011, the Carnegie Institute of Technology B.R. Teare Teaching Award for 2013, and the 2015 Semiconductor Industry Association (SIA) University Researcher Award.